Technical report No. 7, 2011

Observations and Analysis of Sea Ice Motion with the Ice Buoy DRIVA during the 2010 Spring Field Campaign in the Bay of Bothnia

Berg, A., Eriksson, L. E. B., Borenäs, K., Lindh, H.

Department of Earth and Space Sciences
Chalmers University of Technology
Gothenburg, Sweden

Abstract

The ice drift buoy DRIVA is tested for the first time in the environment for which it was designed. The communication with the buoy via satellite phone is working well. Temperatures could be read during the entire test period, and except from an unexplained loss of GPS data during 20 days, the GPS position was transmitted as expected. The rotary encoders did not function properly during the campaign.

A sea ice drift algorithm is validated against the buoy data using ten image pairs acquired by the C-band SAR satellite ENVISAT. The accuracy of the algorithm decreases with time and highest accuracy is achieved with the first three image pairs. For the first image pair, the computed translation differs by only 160 m from the translation measured by the buoy, which is a good result considering the pixel resolution of approximately 150 m. The root mean square error of the algorithm for the first three image pairs is 5% for the ice speed and 4 degrees for the direction of the ice.

The decreasing accuracy can be related to an increase of melting during the campaign. The sea ice is very dynamic during the period, making the images very different. Large ice floes break into smaller pieces after a short time. As the ice floes melt and get smaller, rotation increases, and the shapes of the ice floes are not preserved. It appears that the buoy floats within a streak of slush ice during the last days of the time period. Tracking of the ice is more difficult under such circumstances, because the contours of an area of slush ice are constantly changing.

Contents

1 Introduction

Improved monitoring of sea ice conditions, provided by new satellite products, are of importance not only for winter navigation, but also for assessing changes in the climate. For this purpose data from the radar satellites Radarsat-2, ALOS, Envisat and Cryosat-2 may be used to improve the estimations of sea-ice parameters like ice concentration, ice drift and ice thickness.

In the project ClimatIce, satellite products will be derived that can be used to validate existing climate models, with focus on the Arctic region. The first phase of the project comprises the development of an ice drift algorithm which will be validated against in situ data. For this purpose data from a field campaign with the ice drift buoy DRIVA, will be used. The buoy can provide long time series of GPS positions that will ensure satellite image coverage can be repeated many times. The buoy has potential to also measure the bearing, which will give the rotational movement of the ice.

The buoy was deployed in the Bothnian Bay during the spring 2010 and in this report a summary of the field campaign is presented as well as a description of the DRIVA buoy.

2 Background

2.1 Using buoy data to validate satellite derived sea ice drift

There are few Earth-based methods to measure sea ice drift. Each method has its advantages and limitations when it comes to spatial and temporal coverage, accuracy of measurements, cost of equipment, amount of field work, technical complexity etc. Deployment of drift buoys is an effective way to provide measurements of sea ice drift. The measurements are very accurate and can be made continuously in time. The method is naturally very limited when it comes to spatial coverage because the measurements are point-wise. The start position of the buoy is critical; a good start position may provide a long time series of data whereas an unfortunate position may result in the buoy not moving at all or immediately get stuck in the fast ice or ashore.

Buoy measurements give a Lagrangian description of the drift field, which means that the observed motion is a function of time and buoy position. The ice drift algorithm, on the other hand, gives an Eulerian description of the drift field where the drift is a function of position in time and space. Some limitations follow a comparison based on these two different types of specification. See Figure 1 for an example. The buoy is placed close to the edge on a rotating ice floe. The ice drift algorithm may not find out the rotation of the floe but still keep track of its outline. Thus it will measure the drift of the “centre of mass” of the ice floe. In contrast, the buoy will measure the average drift of the ice floe, but with an offset due to the rotation. The offset is a sinusoidal function of the rotation experienced by the buoy.

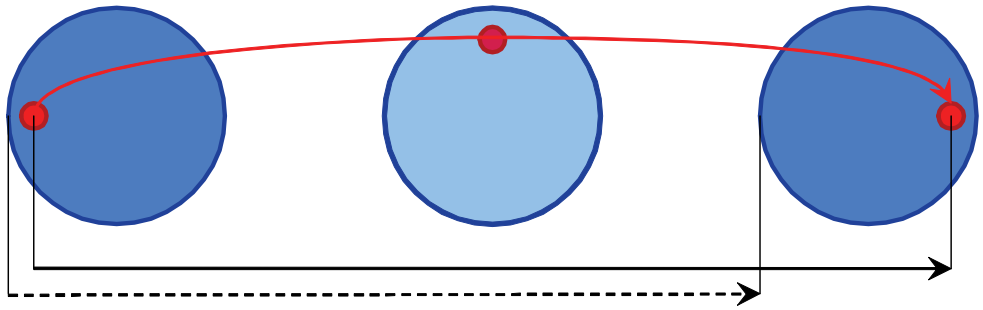

Figure 1. A circular ice floe (large disk) drifts from left to right while rotating clock-wise. The solid arrow corresponds to the drift measured by the buoy (small disk), whereas the dashed arrow corresponds to the drift measured by the algorithm.

2.2 The DRIVA buoy

The DRIVA buoy was constructed at SMHI with the primary goal to create a platform that could transmit ice information in real time for assimilation into operational ice models.

The DRIVA is designed like a barrel. It is made by polyethylene plastic and the weight is about 70 kg. The interior of the buoy is shown in Figure 2. Inside the buoy a Campbell data logger is installed together with an IRIDIUM satellite modem. Sensors for position, air temperature and ice temperature are added. There is also a Gyro Enhanced Motion Sensor installed in the buoy, which

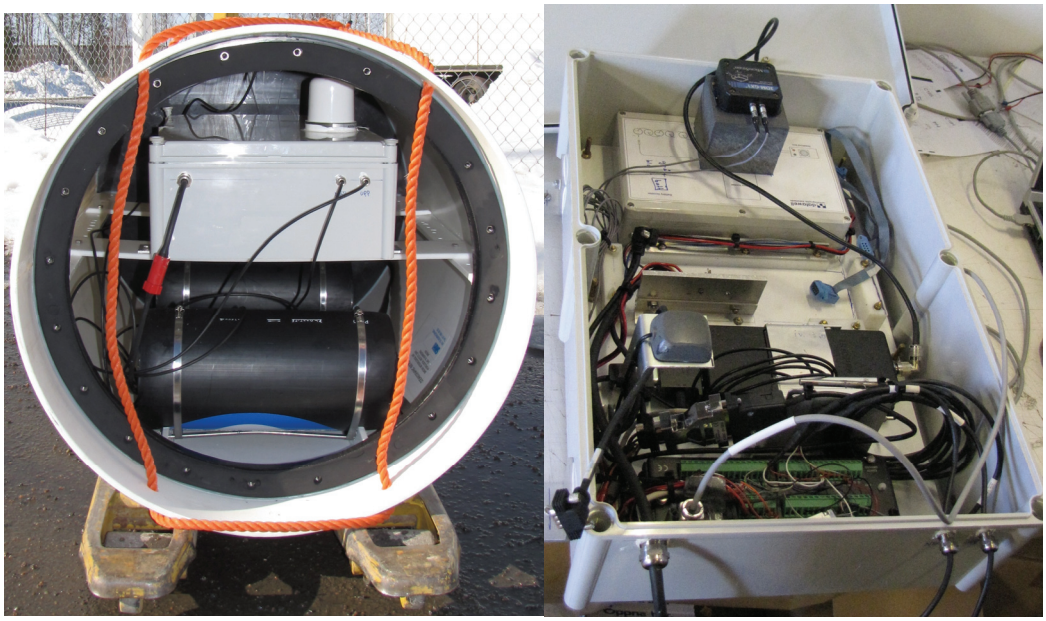

Figure 2. The interior of the buoy. The instruments are installed in the waterproof white box.

measures pitch, yaw, roll and other parameters. The idea was to use this sensor to find out if it is possible to decide whether DRIVA is floating around in open water, lying on an ice-floe or possibly on/in an ice-ridge. The internal battery-pack can have the equipment running for at least one year.

2.3 Deployment

On April 14, 2010, the buoy deployment was carried out. The buoy was flown by helicopter from Umeå to a location in the middle of the Gulf of Bothnia (64°47'N 22°57'E), approximately 65 km off the Swedish coast and nearly 75 km off the Finnish coast. The landing site was chosen on a large ice floe with no ice leads in the vicinity.

The buoy was placed on a tarpaulin to make it visible from a greater distance. To prevent that the buoy was moved by the wind, it was equipped with a sea anchor drifting at a depth of five meters. An image of the setup is shown in Figure 3. Four holes were drilled in the ice at distances less than 100 m from the buoy, and the ice thickness was measured to 40 - 60 cm.

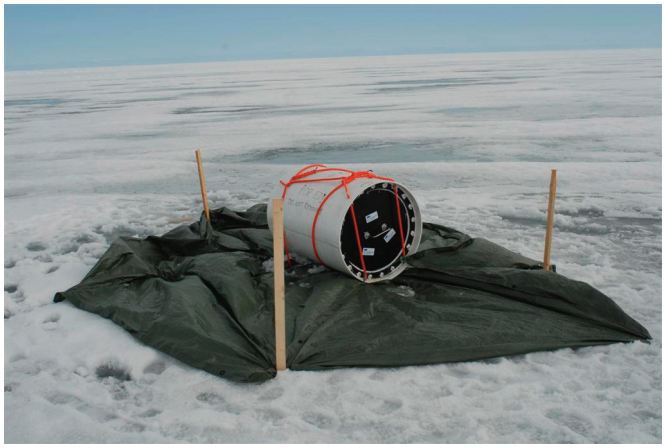

Figure 3. DRIVA in position.

2.4 DRIVA in operation

This section will give a brief summary of the course of events after the buoy was placed in position. Table 1 lists the most important events during the campaign, while Figure 4 shows a map with the track of the buoy.

The sensors in the buoy have a sampling rate of 30 minutes, and transmit data every third hour. If the transmission fails, data is accumulated until next transmission attempt. The data were received at Chalmers by a laptop connected to a GSM modem.

The buoy was working as expected for almost four days, when the buoy stopped transmitting its GPS position. There was no explanation to the failure, but it seemed to be related with the GPS receiver itself, and not a power issue. The other parameters were still transmitted as normal. The malfunction of the GPS device lasted for 21 days, when the GPS position suddenly was transmitted again.

Table 1: Important event during the campaign

Date	Time after deployment	Event
14 April 2010, 11:30 UTC	0 h	The buoy is deployed.
18 April 2010, 07:00 UTC	3 days, 19 hours	Transmission of the GPS position stops.
09 May 2010, 09:30 UTC	24 days, 22 hours	Transmission of the GPS position resumes.
10 May 2010, 14:30 UTC	26 days, 3 hours	The buoy is picked up by the Swedish Maritime Administration, and moved to a new position.
25 May 2010, 23:00 UTC	41 days, 11 hours	Last temperature measurement below 0° C.
05 June 2010, 04:00 UTC	51 days, 16 hours	Transmission of the GPS position stops.
05 June 2010, 12:08 UTC	52 days, 0 hours	The buoy is picked up by the Finnish Coast Guard.

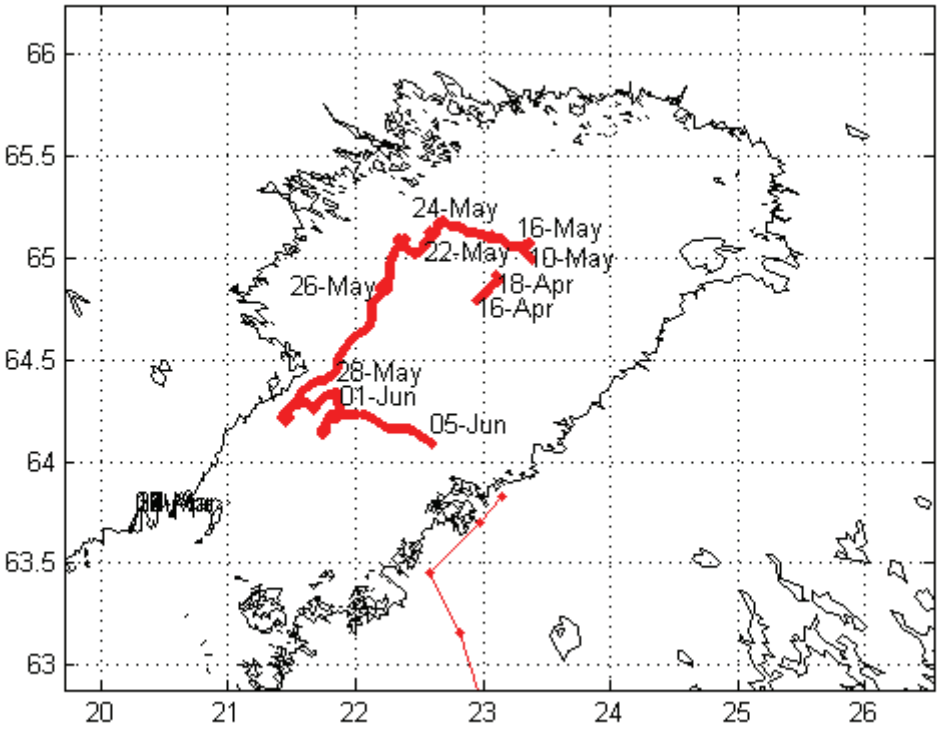

Figure 4. Drift of the ice buoy. The buoy was deployed in 64°47'N 22°57'E.

2.5 Sea ice conditions during the campaign

During March, westerly winds dominated the Bay of Bothnia and pushed the pack ice towards Finland [1]. The buoy was deployed two weeks into April. At this time, the eastern side of the ice cover was characterized by ridges and hummocked ice, whereas a large ice lead took form on the western side. The ice cover had reached its maximum thickness of 40-70 cm in the region of the buoy [2]. The melting season had already lasted for a couple of weeks in southern Sweden, and the archipelago ice south of Stockholm had melted completely.

The melting was of small extent in the Bay of Bothnia during April and the beginning of May. The fast ice began to rotten the first days of May at latitudes north of Umeå. The solid pack ice started to break up around May 6-9. The breakup was forced a bit further by the episode of the ship that was sent to pick up the buoy on May 10. The ship created a lead nearby the buoy, and thus exposed the surrounding ice to melting (Figure 5).

Melting accelerated during the next four days, as very warm weather arrived from the east. In Haparanda, at the northernmost part of the Gulf of Bothnia, the temperature was measured to more than 25 °C three days in a row. The ice field became even more fragmented and started to drift to the southwest. On May 16, the archipelagoes in the Bay of Bothnia rapidly turned ice free. The conditions at sea were rather mixed with elements of rigid ice floes, rotten pack ice, floebits, and belts of drifting slush ice. By the end of May the ice cover was fully dissolved.

2.6 Acquired satellite data

A number of Synthetic Aperture Radar (SAR) images were acquired during the field campaign. ENVISAT ASAR was used for regular observation, while TerraSAR-X and Cosmo-SkyMed were used to acquire high-resolution data at three occasions. Table 2 lists all images obtained with ENVISAT ASAR during the campaign. The GPS was malfunctioning for a period of three weeks. During this time period images were acquired less frequently. All images were acquired in HH polarization, with the exception of one image that was acquired in VV polarization during the GPS failure.

Totally, 22 ASAR images are available before the buoy with certainty started to float in open water. Position data from the buoy is available for 13 of these images. At one occasion the buoy was moved to a new position, which makes the buoy data of no use for validation. In the end there are 12 images, or 10 image pairs, that can be used to validate the computed ice motion, of which one image pair is from before the GPS failure, and the remaining nine image pairs are from the subsequent period. The corresponding images are shaded in the table.

Table 2. Flyovers of ENVISAT ASAR in Wide-Swath Mode.

Date and time (UTC)	Pol.	GPS position	Orbit nr	Asc./ Desc.	Notes
13-Apr-2010 09:14	HH	Yes	308	D	Buoy not yet deployed
15-Apr-2010 19:40	HH	Yes	343	A	
16-Apr-2010 09:18	HH	Yes	351	D	
17-Apr-2010 08:48	HH	No	365	D	
18-Apr-2010 19:45	HH	No	386	A	
20-Apr-2010 08:54	HH	No	408	D	
24-Apr-2010 19:56	HH	No	472	A	
27-Apr-2010 20:02	HH	No	014	A	
01-May-2010 19:37	HH	No	071	A	
05-May-2010 09:19	VV	No	079	D	
06-May-2010 08:51	HH	No	136	D	
09-May-2010 08:57	HH	No	179	D	Buoy position transmitted 30 min. later
10-May-2010 19:54	HH	Yes	200	A	Buoy was moved before fly-over
12-May-2010 09:03	HH	Yes	222	D	
13-May-2010 19:59	HH	Yes	243	A	
15-May-2010 09:09	HH	Yes	265	D	
16-May-2010 20:05	HH	Yes	286	A	
17-May-2010 19:34	HH	Yes	300	A	
18-May-2010 09:14	HH	Yes	308	D	
20-May-2010 19:40	HH	Yes	343	A	
21-May-2010 09:20	HH	Yes	351	D	
23-May-2010 19:45	HH	Yes	386	A	

Figure 5 and Figure 6 show image frames from each of the twelve ASAR images, centered on the buoy position. Contrast stretching has been performed individually for each window. Each window covers an area of 20 by 20 kilometers.

One X-band TerraSAR-X image was ordered during the campaign and is shown in Figure 7. It was acquired in HH-polarized ScanSAR mode at roughly 20 m resolution, one day after the buoy was deployed, on April 15th, 2010, at 05:04 UTC. The image clearly depicts the ice floe on which the buoy was deployed. Two X-band Cosmo-SkyMed images were ordered. The first image was obtained on April 25th, 2010, at 17:18 UTC, in StripMap mode at 5 m resolution and in HH-polarization. The image was ordered because the buoy position was not known at that moment and it was decided to approximate the position from the characteristics of the surroundings. The second image was acquired on May 31st, 2010, at 18:30 UTC, in StripMap mode with dual polarization (HH and HV), and at ground range resolution of 20 m.

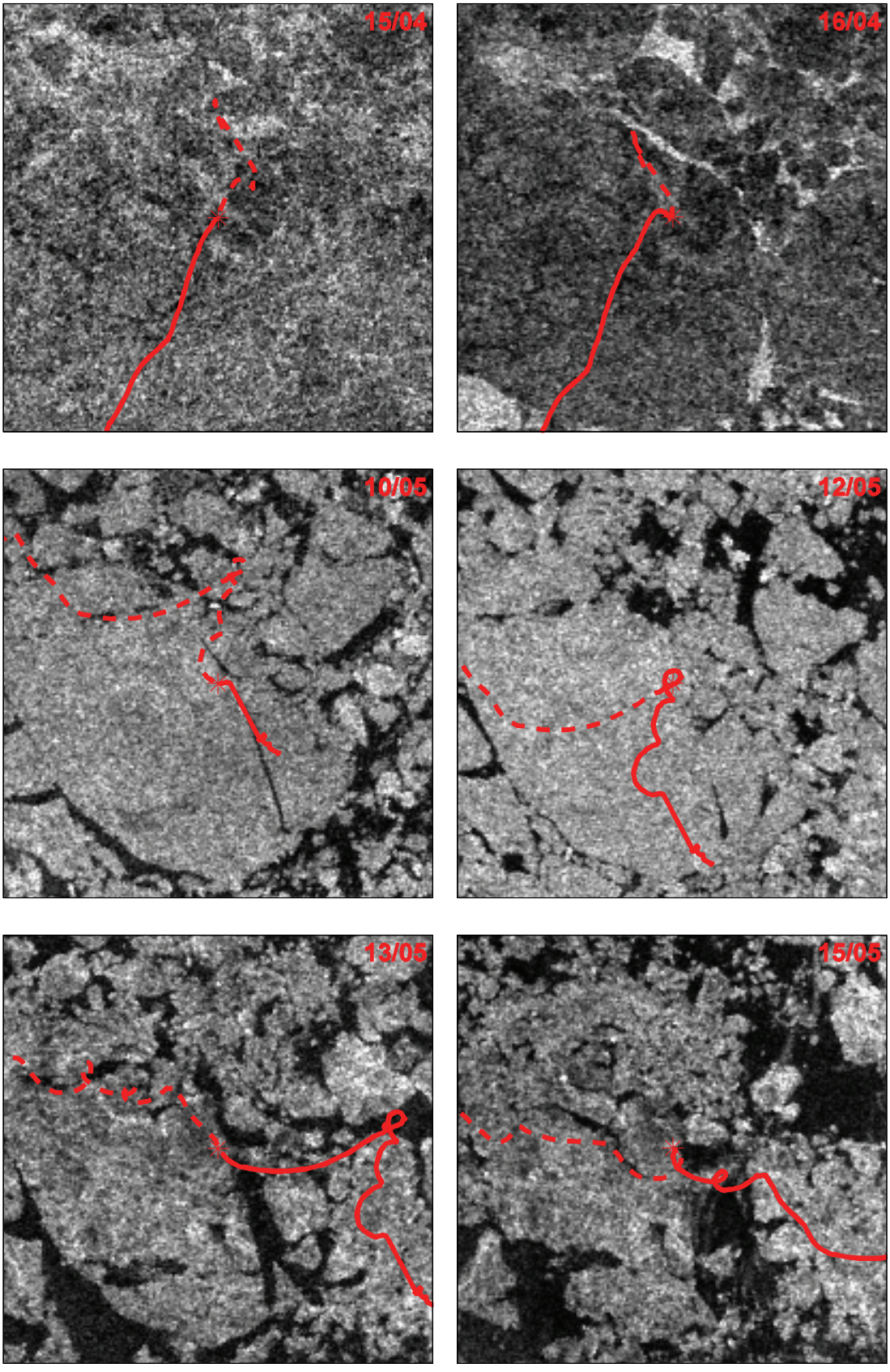

Figure 5. Image windows from the first six ASAR images, centered on the buoy position (marked with asterisk). Solid lines represent the buoy track before image acquisition, and dashed lines represent the buoy track afterwards.

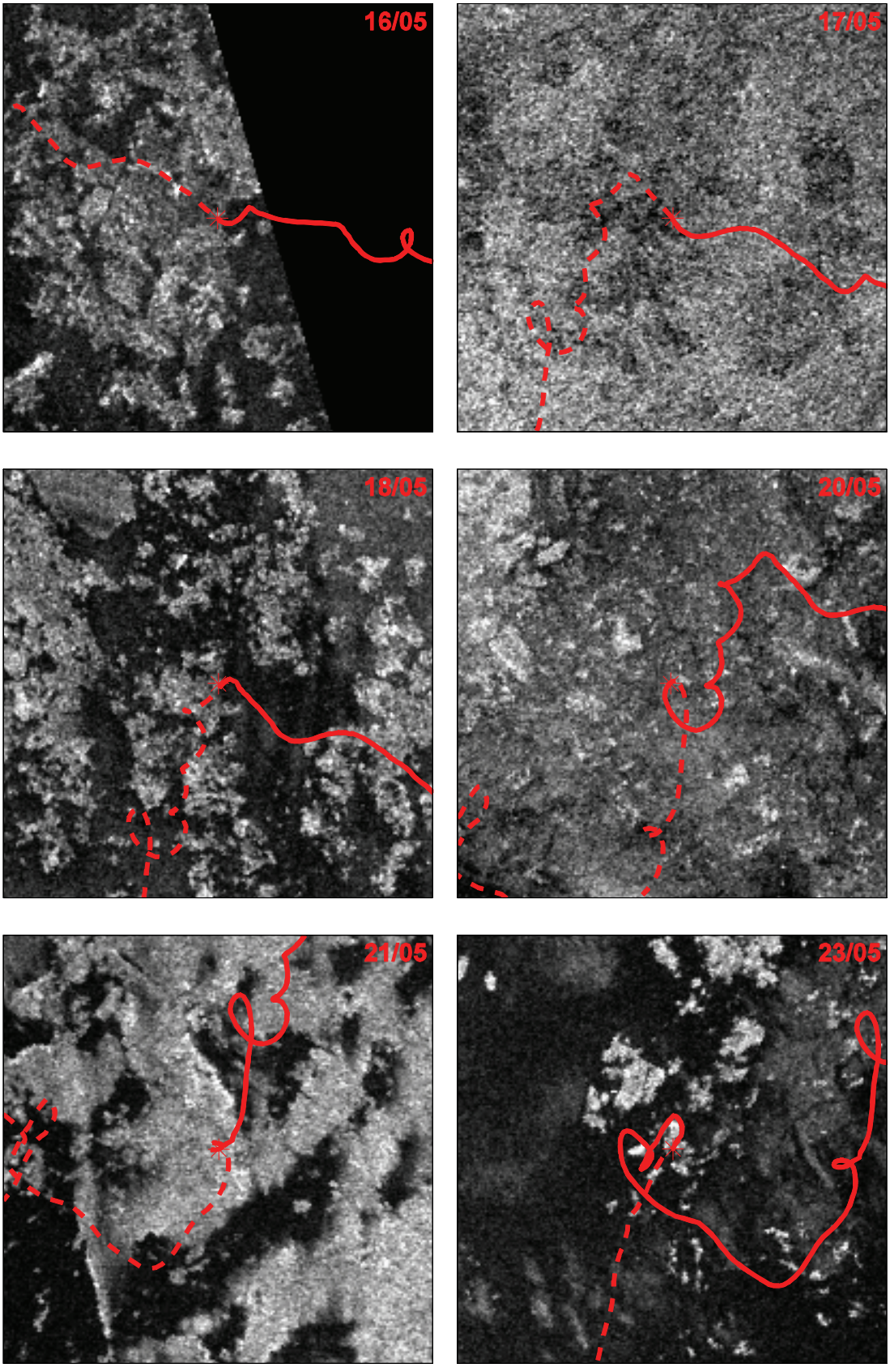

Figure 6. Image windows from the last six ASAR images, centered on the buoy position (marked with asterisk). Solid lines represent the buoy track before image acquisition, and dashed lines represent the buoy track afterwards.

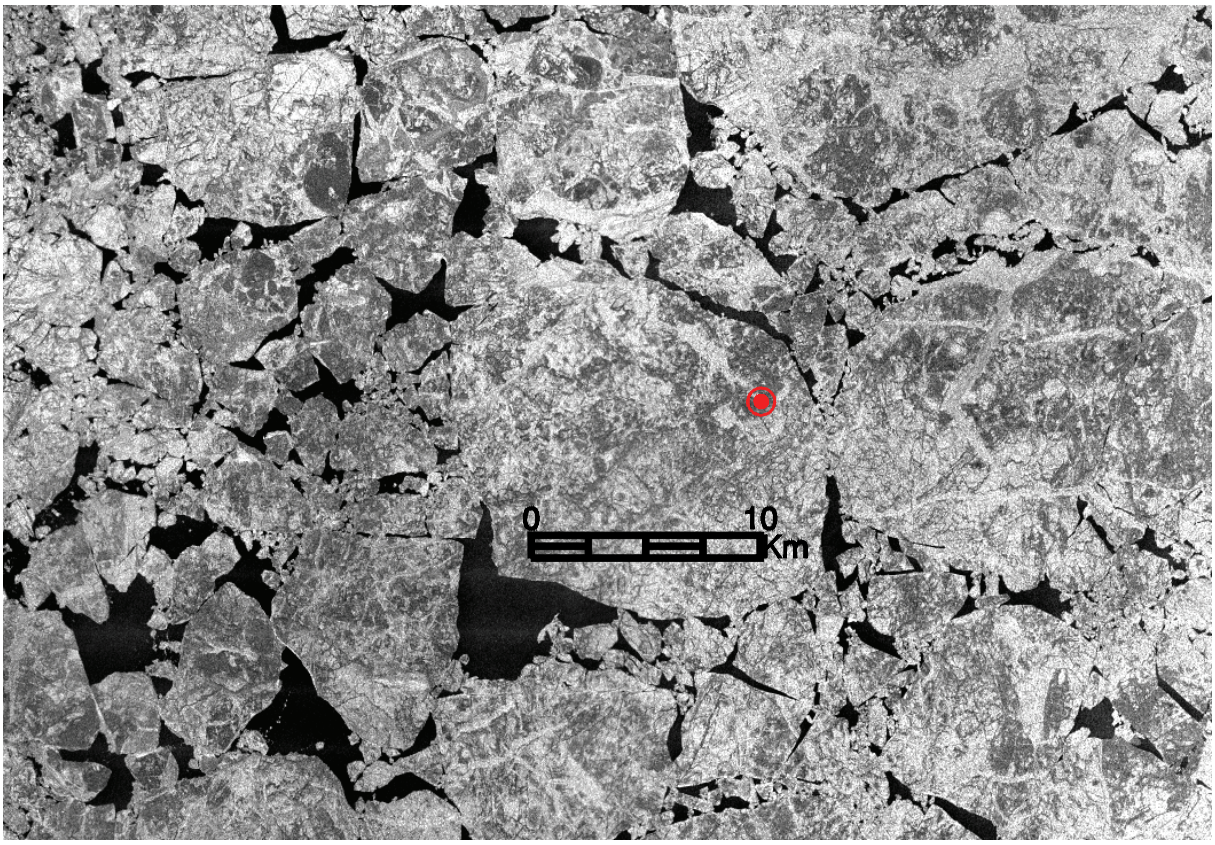

Figure 7. HH-polarized TerraSAR-X ScanSAR image acquired on April 15, 2010, at 05:04 UTC. The red dot marks the position of the ice buoy, at roughly 2 km from the edge of the ice floe.

3 The sea ice drift algorithm

The sea ice drift algorithm used in this study is a development of the algorithm described in [3]. The basic method of using phase correlation is still the same, as is the multi-resolution approach, but some important changes have been made to the algorithm. The grid-based data storage is replaced by a point-wise representation, a land mask has been incorporated into the algorithm, and an approach to determine the rotation has been implemented.

3.1 Theory

Phase correlation

Phase correlation [4] is the central part of the algorithm. Given two images f_1 and f_2, f_2 will be translated in respect to f_1 according to $f_2(x) = f_1(x - d)$ using a one-dimensional notation. According to the Shift theorem, a (circular) shift of a function corresponds to a multiplication of its Fourier transform by a linear phase. Thus, the Fourier transform of f_2 equals $F_2(\xi) = F_1(\xi)e^{-2\pi i d\xi}$. A multiplication of this expression with the complex conjugate of $F_1(\xi)$ will cancel out the phase

information from the original image. The phase will then be determined by the translation d. In this way the cross-power spectrum

$$R(\xi) = \frac{\overline{F_1(\xi)}F_2(\xi)}{\left|\overline{F_1(\xi)}F_2(\xi)\right|} = \frac{\overline{F_1(\xi)}F_1(\xi)e^{-2\pi i d\xi}}{\left|\overline{F_1(\xi)}F_1(\xi)\right|} = e^{-2\pi i d\xi} \tag{3.1}$$

is obtained. Note that the magnitude components are eliminated, which makes the method illumination invariant. The cross-power spectrum can be inversely Fourier transformed to a Dirac delta function as $r(x) = \mathcal{F}^{-1}\{R(\xi)\} = \delta(x - d)$. From this result the translation is computed as $d = \text{argmax}_x\, r(x)$.

The phase correlation differs from the normalized cross-correlation in that the Fast Fourier Transform can be used with a large reduction of computational load.

Phase correlation is limited in the sense that it only measures *cyclic* shifts. This is a consequence of the wrapping effect of the Fourier transform. In reality, the shift between the two images is not cyclic because something that drifts out of the image at one side does not appear at the other side. For that reason one will not obtain an impulse function but the impulse will degenerate into a peak. Also, because the images are not periodic, discontinuities from left to right boundaries and from top to bottom boundaries will introduce ripples in the frequency domain. These ripples are reduced by blurring the image edges. The blurred edges are smoothly transformed into the original image in the center part.

With the assumed periodicity follows a limitation on the maximum range of displacement. A displacement that extends beyond half the size of the image block along a spatial direction will not be detected. The multi-resolution approach used by the algorithm is a way of overriding this limitation. The resolution is decreased in order to have geographically larger image blocks. The algorithm starts at the lowest resolution level where the largest displacements can be detected.

Rotation determination

A rotation between image f_1 and f_2 can be determined by a Fourier-Mellin transform of the images [5, 6]. The transformation is a mapping of the images in frequency domain. Starting with the images in spatial domain, the image $f_2(x, y)$ is a translated and rotated replica of image $f_1(x, y)$, as

$$f_2(x, y) = f_1(x \cdot \cos\,\theta_0 + y \cdot \sin\,\theta_0 - x_0, -x \cdot \sin\,\theta_0 + y \cdot \cos\,\theta_0 - y_0)\,, \tag{3.2}$$

where the rotation $\theta_0$is counted counter-clockwise. The translation and rotation properties of the Fourier transform yields

$$F_2(u, v) = e^{-j2\pi(ux_0+vy_0)} \cdot F_1(u \cdot \cos\,\theta_0 + v \cdot \sin\,\theta_0, -u \cdot \sin\,\theta_0 + v \cdot \cos\,\theta_0)\,. \tag{3.3}$$

The log-polar transformation is a mapping of coordinates (u, v) in the Cartesian plane to (ρ, θ) coordinates in the log-polar plane defined by

$$\begin{cases} \rho = \log\left(\sqrt{u^2 + v^2}\right) \\ \theta = \operatorname{atan}\left(\frac{v}{u}\right) \end{cases} \tag{3.4}$$

Applying the transformation on F_1 and F_2 and taking the absolute value gives

$$M_1(\rho, \theta) = M_2(\rho, \theta - \theta_0). \tag{3.5}$$

It can be seen in the expression that the rotation has been transformed into a translation. The rotation θ_0 can in principal be recovered by a second phase correlation, but another method will be used in this study.

The Mellin transform makes the radial component of the coordinate system logarithmic and therefore scale invariant. The scale invariance can be demonstrated by taking image f_2 as a spatially scaled replica of f_1 with scale factor a, so that $f_2(x, y) = f_1(ax, ay)$. The Fourier transforms of f_1 and $f_2$are then related by

$$F_2(u, v) = \frac{1}{a^2} F_1(u/a, v/a) \tag{3.6}$$

in accordance with the scale property of the Fourier transform. If (u, v) is scaled to $(u/a, v/a)$, it can be represented in a log-polar coordinate system by

$$\begin{cases} \rho = \log\left(\sqrt{(u/a)^2 + (v/a)^2}\right) = -\log \mathrm{a} + \log\left(\sqrt{\mathrm{u}^2 + \mathrm{v}^2}\right) \\ \theta = \operatorname{atan}\left(\frac{v/a}{u/a}\right) = \operatorname{atan}\left(\frac{v}{u}\right) \end{cases} \tag{3.7}$$

It is noted that scaling has been reduced to a translational movement along the radial component of the coordinate system. With f_2 as a translated, rotated and scaled version of f_1, the magnitude of F_2 (ignoring the multiplication factor $1/a^2$) is

$$M_2(\rho, \theta) = M_1(\rho - \log\ a, \theta - \theta_0). \tag{3.8}$$

It can be concluded that rotation by an angle θ_0 and scaling by a factor a has become a two-dimensional translation that can be determined using phase correlation.

The scale invariant property of the transformation is not employed in the current version of the algorithm. It is instead assumed that scaling does not occur. In order to find the rotation θ_0 a rotation signature function can be defined according to [7]

$$\phi_r(\theta) = \int_{\rho=1}^{\log\left(\frac{N}{2}\right)} J\big(M(\rho, \theta)\big) d\rho, \tag{3.9}$$

where J is a weighting function and N is the sidelength of the quadratic images. The function J acts as a filter that selectively weight certain frequencies (independent of θ) in the magnitude of the Fourier transform. The most important property of the J function is that it minimizes the DC component at

small values of ρ. Instead the filter puts emphasize on the range of frequencies that correspond to the size of ice floes and higher frequencies which hold information on ice leads cracks, and noise.

The rotation signature is determined separately for the two images. A cross-correlation is then made in order to find the maximum correlation which correspond to the rotation as

$$\theta_0 = \underset{\theta}{\operatorname{argmax}}(\tilde{\phi}_{r,1} \star \tilde{\phi}_{r,2})(\theta), \tag{3.10}$$

where tilde denotes normalization with subtraction of the mean and division by the standard deviation.

3.2 Algorithm implementation

A block scheme of the algorithm is shown in Figure 8. The processing starts with two quadratic image blocks I1 and I2, extracted from the two original images. The original images are geocoded so that the two subimages cover the same geographical area in the initial stage. The image blocks enter the multi-resolution processing system which is illustrated by a dotted frame in the flow chart. The image blocks are downscaled by a factor that decreases for each iteration. The full resolution is used during the last iteration. Down-scaling is followed by phase correlation in order to find the translational offset between the two blocks. After this has been done for all image blocks, the resulting motion field will be filtered and up-sampled to match the new resolution level. The resolution is made finer in the next iteration. The computed motion field is used to translate image blocks from the second image back to their estimated position in the first image. The image blocks keep their full resolution at the final iteration. If the performance of phase correlation turns out to be low at this stage, an attempt will be made to recover a possible rotation between the two blocks. If the rotation is recovered with high reliability, phase correlation will be performed one more time with the second image block rotated to match the first image block. If this attempt results in a phase correlation that is higher than before, the rotation will be considered as recovered. If the correlation does not get better, the first estimate of the translation will be used.

When all image blocks have been processed in full resolution, the motion field will be filtered using weighted median filtering [8] according to

$$d_{wm}(x_0, y_0) = \underset{d(x,y)}{\operatorname{argmin}} \sum_{(x-x_0)^2+(y-y_0)^2<R^2} (w(x,y)|(d(x,y) - d(x_0, y_0)|\,). \tag{3.11}$$

Here, R denotes the radius of the filter, $w(x, y)$ is the value of the phase correlation and $d(x, y)$ is the estimated translation along an axis. The filter output d_{wm} forms the final motion field.

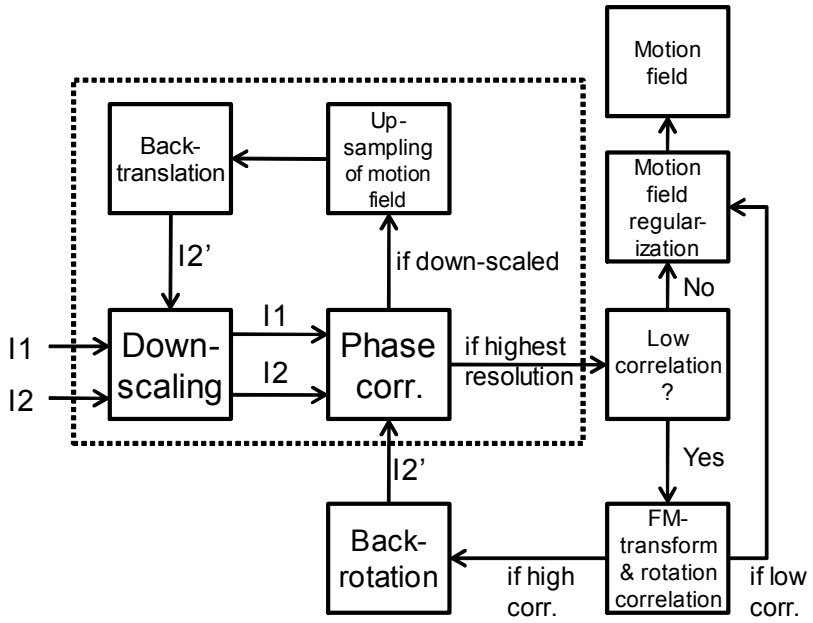

Figure 8. Flow chart of the algorithm. I1 and I2 refer to image block 1 and 2. I2' is an updated block that replaces I2. The framed part of the flow chart is iterated for each resolution level. The flow chart is subject to some simplifications. The processing flow is halted at some stages until all image blocks have been processed and this is not indicated in the chart. Catches are used to avoid otherwise infinite loops.

3.3 Implementation issues

Land mask

A land mask is computed for the first image using data from the Global Self-Consistent Hierarchical High-Resolution Shoreline database [9]. The land mask is constructed from shoreline data in vector format. The vector data is converted to raster data and then to a binary land mask by a flood-fill operation on the ocean surface. The current implementation sets a limit on the number of pixels in the land mask. For images with more than 10^7 pixels, the land mask will be down-scaled to that specific pixel size. A land mask is not required for the second image because processing starts from valid regions in the first image. An image block is considered valid if the land fraction is less than twenty percent.

Down-scaling

Down-scaling is performed by reductions in image resolution by factors of two using a recursive function. The image is filtered with a two-dimensional, rotationally symmetric, Gaussian low-pass filter with a size of 3 pixels and a standard deviation of 1. Spatial filtering is followed by down-sampling a factor two.

Phase correlation

Phase correlation is based on the Fourier transform of images. Leakage appears when the Discrete Fourier Transform (DFT) is applied to images that are assumed to be periodic and infinite. The images

are neither periodic nor infinite and will for that reason give rise to discontinuities. Discontinuities are formed at the image borders because they do not match when aligned to each other. The effect of leakage is seen as ripples in the frequency domain. Image frequencies are spread out, or leaked, to other image frequencies. The effect of leakage is reduced by blurring the image edges. The image is blurred by a point-spread function, and the new image is a weighted sum of the blurred version and the original image. The new image will be weighted so that the blurred image dominates at the edges and the original image occupies the central region.

Fourier-Mellin transformation and rotational ambiguity

The Fourier transform is conjugate symmetric for real valued functions, meaning that $F(x) = F^*(-x)$. The magnitude of the Fourier transform of an image is thus symmetric and has a 180 degree ambiguity. Only one side of the two-dimensional DFT will thus be transformed to log-polar domain. This means that the rotation signatures will have a length of π radians. The transformation is made with nearest neighbor interpolation and uses only pixels from the largest inscribed circle in the two-dimensional DFT. A consequence of the 180 degree ambiguity is that all retrieved rotations are mapped to the interval from -90 to +90 degrees. A rotation of +120 degrees will for example be mapped to a rotation of -60 degrees.

The two-fold rotational ambiguity can be resolved by performing back-rotation followed by phase correlation for each possible solution. This is not implemented in the current version of the algorithm, but instead the rotation is selected within the stated interval. The algorithm is then able to measure rotations up to 90 degrees. This limitation is insignificant if the temporal separation between the images is small and rotations of more than 90 degrees are uncommon.

Weighting the rotation signature

The J filter in Eq. (3.9) is used to bring out spatial frequencies that characterize different ice regions. The filter has been determined empirically, partly by comparing the two-dimensional DFT from different regions, partly by optimizing the filter for some test cases. The Fourier-Mellin transformation cause individual pixels at low frequencies to be turned into multiple pixels in the log-polar domain. It is obvious because the transformation must cover the full angular range with a small amount of pixels. As a result, the DFT will appear as pixelized at low frequencies in the log-polar domain. The correlation of rotation signatures is very sensitive to this effect. The location of the boundaries between pixel “groups” (where one group of pixels originate from a single pixel in the original domain) has a large impact on the correlation, also due to the fact that the magnitude of the DFT is relatively high at low frequencies. The filter is designed to compensate for this effect by suppressing lower frequencies and level the magnitude of the DFT over the frequency bandwidth. It would be possible to further tune the J filter by creating a large set of test data with simulated rotations.

4 Results

4.1 Drift of the buoy

The daily drift of the ice buoy can be seen in Figure 9. Around May 20, roughly one month after the deployment, the movement of the buoy became significantly larger. This occurred as the pack ice started to break up. The buoy started to drift westwards, and on May 25 the last temperature below the freezing point was measured. Satellite images from ENVISAT ASAR revealed the buoy was drifting in a swathe of trash-ice for a short period until it was completely surrounded by water.

After that, the buoy drifted around 80 km southwards followed by an eastward movement of roughly 50 km, until it was eventually picked up by the Finnish Coast Guard and sent back to SMHI in Norrköping.

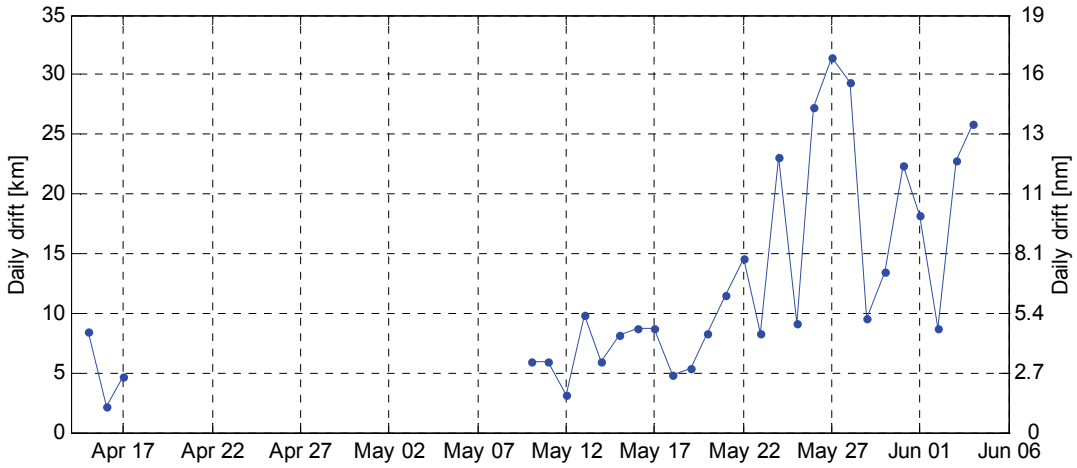

Figure 9. Daily drift of the ice buoy.

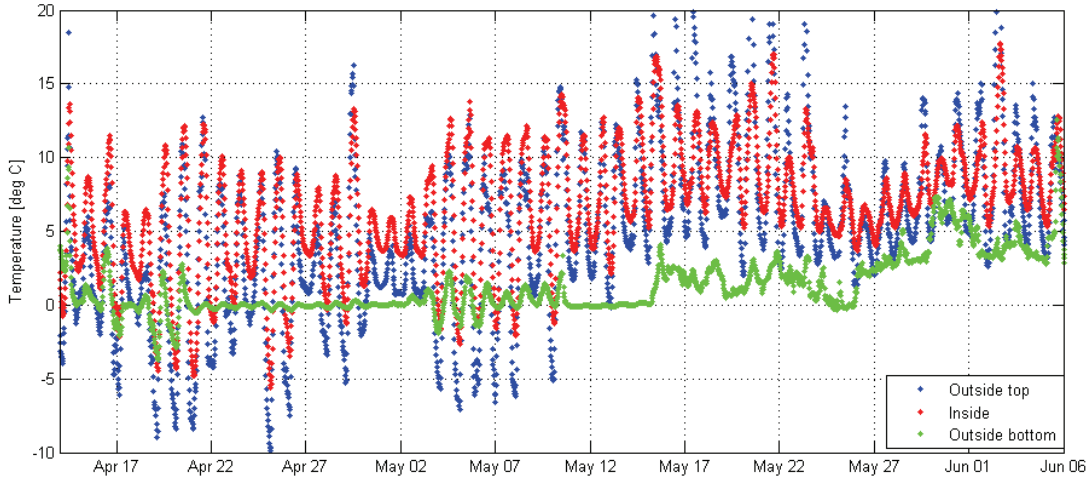

Figure 10. Temperature from the three sensors.

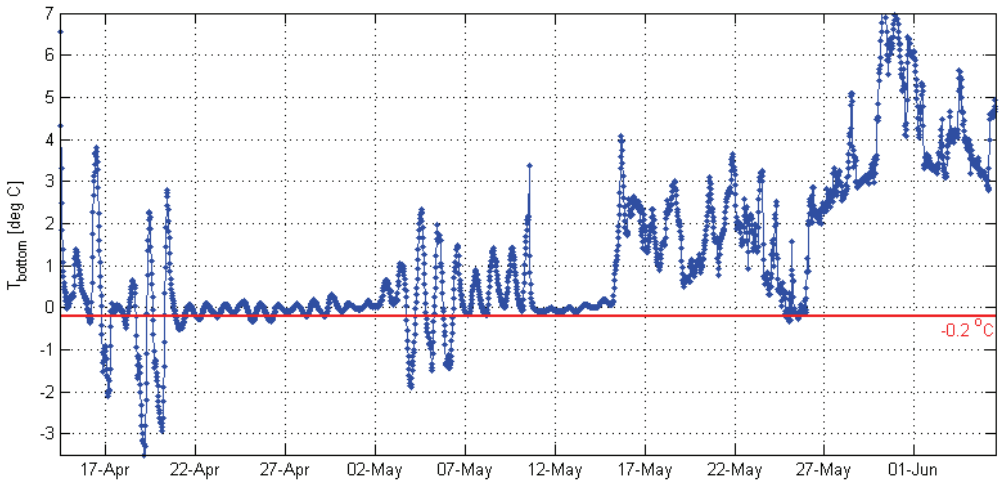

Figure 11. Temperature on the outside bottom. The freezing point is around -0.2 °C.

4.2 Transmitted data

The data transmitted by the buoy consist of 17 fields listed in the appendix. The transmitted parameters include *date and time*, *GPS position*, *temperature data* from three thermometers, *angular position* from rotary encoders and *battery voltage*.

The temperature is measured by three thermometers. Two of them measure the outside temperature on the top and at the bottom of the buoy, respectively, and one is used to measure the temperature inside the buoy. The temperature data from the period when the buoy was drifting are plotted in Figure 10.

The temperatures measured on the top and inside the buoy follow each other very well, with a Pearson's correlation coefficient of 0.90. The inside temperature is fluctuating less though; the coldest temperature measured inside was -5.6 °C, while it was -9.9 °C on the outside.

It is difficult to determine exactly the time when the buoy started to float in water based on the temperature data. After May 14, there was a period of nearly 10 days when the bottom temperature was fluctuating around 2 °C. It is possible that the buoy was floating in slush ice during this 10-day period. Then, on May 25, the bottom temperature turned below the freezing point for one day and night - this was the last temperature measurement below 0 °C. After May 25, it is certainly the case that the buoy floated in water. Figure 11 shows how the temperature underneath the buoy varies above the freezing point of approximately -0.2 °C.

Before the buoy was deployed, it was found that the rotary encoders gave incorrect values. Figure 12 shows the angular position data that were transmitted by the buoy. Every twelfth hour, the angular positions jump to zero, and after about 2-3 samples the values are back at the original positions. It was also found that the angular position is strongly correlated with the outside temperature, as shown in Figure 13. So far we do not have any explanation to this strange result.

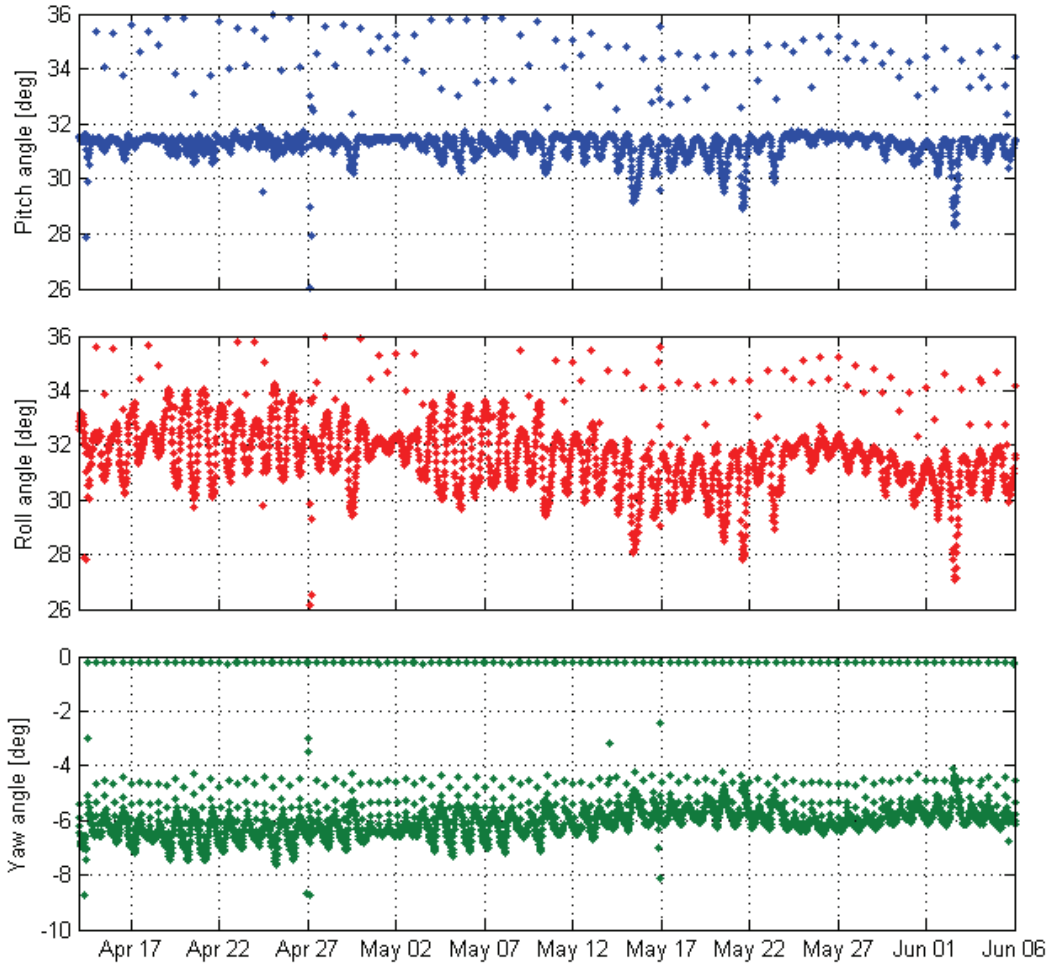

Figure 12. Pitch, roll and yaw angles.

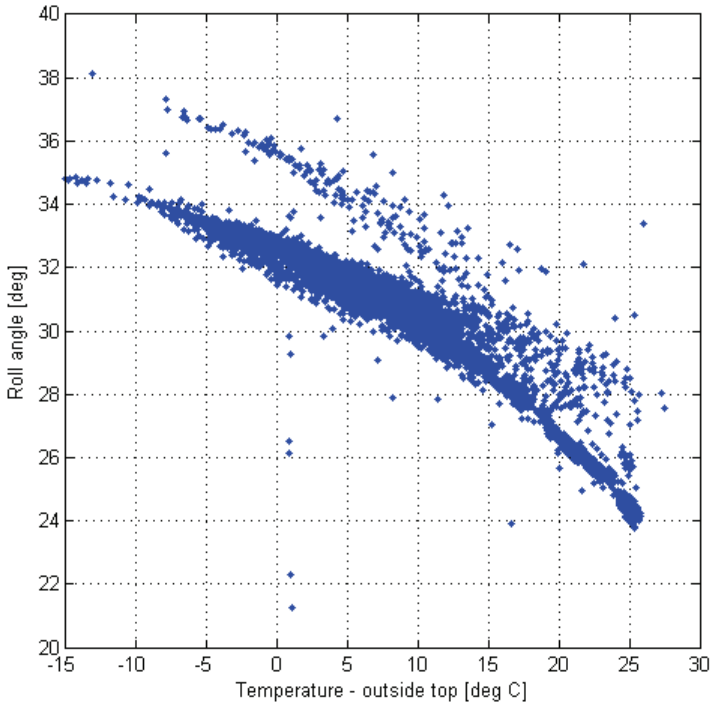

Figure 13. Roll angle versus outside temperature.

The battery voltage was very stable during the entire test campaign, with a mean value of 12.05 V. Figure 14 shows the battery voltage over four months, including the time period of the test campaign.

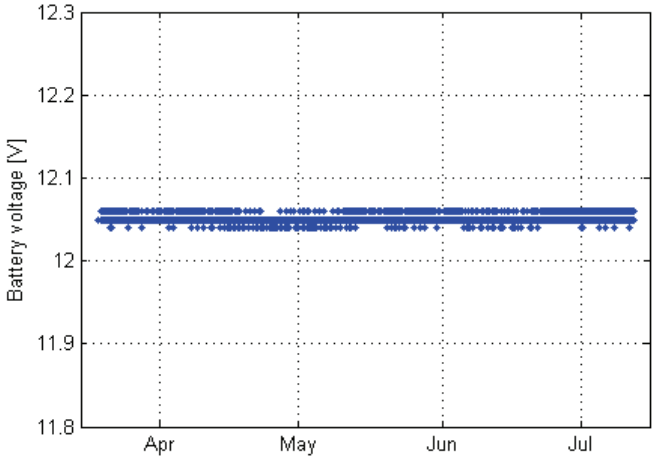

Figure 14. Battery voltage.

4.3 Results of drift algorithm

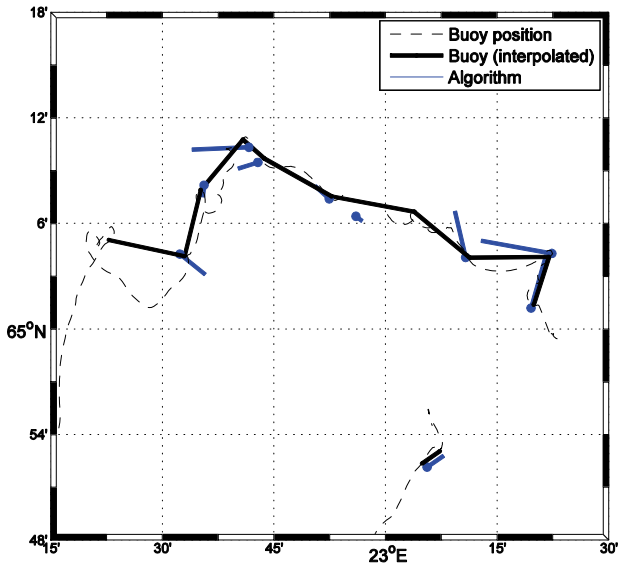

Figure 15. Buoy position is shown both directly and interpolated at the twelve occasions of satellite fly-overs. The computed ice drift is presented at the point in the data set that is closest to the buoy. The buoy enters from the south and drifts to the west.

Figure 15 shows the GPS position measured by the buoy along with the computed ice motion. The ice motion is presented as a line between a pair of coordinates in each image. The position in the first

image is selected as the point in the data set that is closest to the buoy, and the new position in the second image is computed based on the estimated drift.

It can be noted that the computed drift corresponds very well to the motion of the buoy in the first two image pairs. For the first image pair, the measured drift direction of 55.0 degrees east of north is very close to the computed drift direction of 55.4 degrees. The measured translation is 2.28 km and the computed translation is 2.12 km, a difference of 6.7 percent. The accuracy starts to decrease for the third image pair. The magnitude of the drift differs by 9.5 percent and the estimate drift direction has an offset of 10 degrees. The accuracy of the computed drift is slightly worse for the fourth image pair. The direction differs by 37 degrees and the magnitude of the drift differs by more than 30 percent. Table 3 shows the errors of the algorithm when the computed ice drift is compared against buoy data.

The decreasing accuracy can be related to an increase of melting during the campaign. The sea ice is very dynamic during the period, creating too many differences between the images. Large ice floes break into smaller pieces. The ice floes melt and get smaller, rotation increases, and the shapes of the ice floes are not preserved. From the satellite images it appears that the buoy floats within a streak of slush ice. Slush ice is even more difficult to track because the contours of an area of slush ice are constantly changing.

The algorithm tried to resolve the rotation between the images for all the ten cases. The correlation of the rotation signatures was not good enough to meet the requirements for a back-rotation. The requirements are set relatively high to minimize computational load. They can be relaxed at the expense of more “false alarms”, i.e. cases where the rotation is incorrectly determined and back-rotation is performed unnecessarily. Highest correlation was reached with the first image pair for which the rotation was estimated to -6 degrees.

Table 3. Accuracy of the computed ice motion at the position of the buoy. Absolute and relative errors are given in reference to buoy data. Also given is the peak value of the phase correlation and the mean temperature beneath the buoy.

Date of first image	Drift error				Direction error	Corre-lation	Mean temp. beneath buoy
	$\lvert v_{alg}\rvert-\lvert v_{buoy}\rvert$	rel. $\lvert v_{buoy}\rvert$	$\lvert v_{alg}-v_{buoy}\rvert$	rel. $\lvert v_{buoy}\rvert$			
	[cm/s]	[%]	[cm/s]	[%]	[deg]	[-]	[°C]
Apr 15	-0.3	-7	0.3	7	0	0.133	0.4
May 10	0.3	9	0.4	9	-2	0.057	-0.1
May 12	-0.6	-10	1.3	20	11	0.046	-0.0
May 13	-1.9	-34	3.5	62	37	0.060	0.1
May 15	-6.4	-91	7.6	108	-154	0.053	2.3
May 16	-7.3	-75	7.4	76	13	0.055	1.6
May 17	-1.7	-27	5.4	89	-59	0.057	1.8
May 18	-0.4	-14	2.5	77	48	0.069	1.6
May 20	-12.1	-83	12.2	83	-8	0.052	1.5
May 21	-2.2	-58	5.4	139	-153	0.049	2.1

An example of the motion field computed by the sea ice drift algorithm is shown in Figure 16, using the first image pair from April, 2010. Areas of fast ice are easily distinguished. The ice drift is mainly eastwards, or to the northeast in the eastern parts.

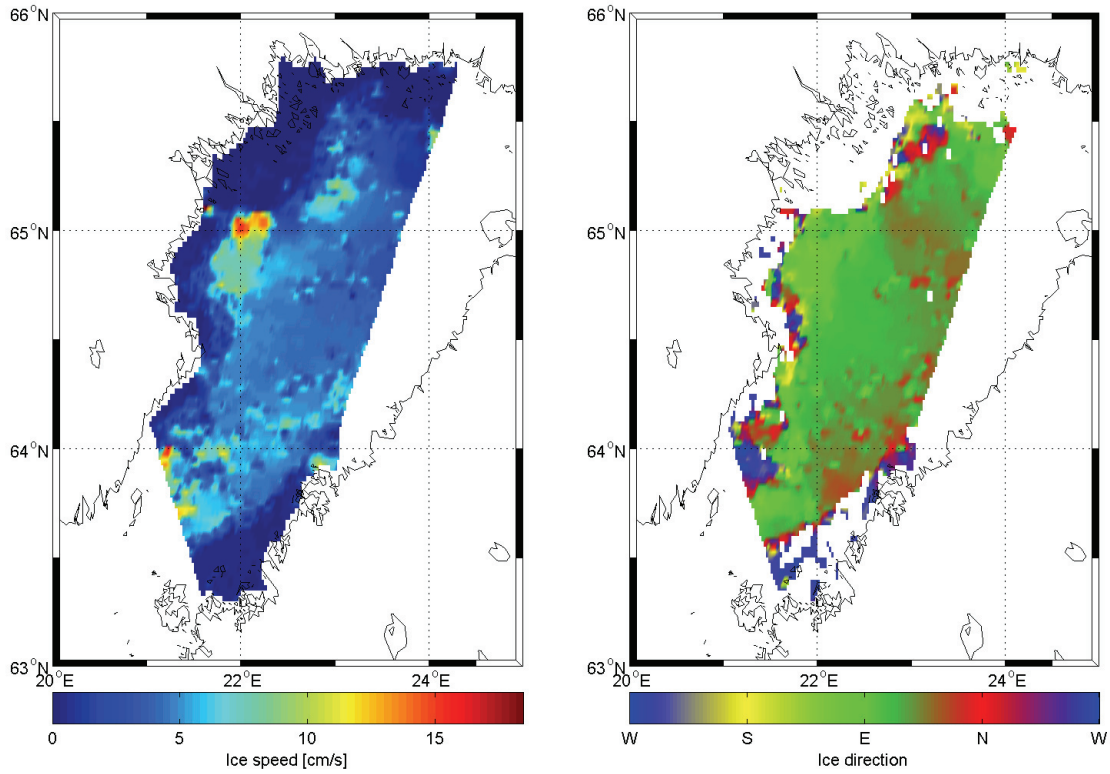

Figure 16. Ice speed and ice direction computed by the algorithm for the first image pair (Apr 15-16, 2010). The direction is shown for translations of at least 200 m. and is otherwise masked out.

5 Conclusions

The ice drift buoy DRIVA has been tested for the first time in the environment for which it was designed. The communication with the buoy via satellite phone was working well. Temperatures could be read during the entire test period, and except from an unexplained loss of GPS data during 20 days, the GPS position was sent as expected. Unfortunately, the rotary encoders did not function properly. The cause of this problem must be investigated further before the buoy is set into work again.

The deployment of the buoy was unfortunately delayed, and as a result it was put into operation relatively late in the ice season. Still, the results show that the buoy is useful for ice drift measurements and that the data from DRIVA can be used to validate ice drift information derived from satellite images.

The sea ice drift algoritm was validated with ten image pairs from the ENVISAT satellite that simultaneously cover the buoy. The accuracy of the algorithm decreases with time and highest accuracy is achieved with the first image pair. In that case the computed translation differs by only 160 m from the translation measured by the buoy. It is a very good result considering the offset is slightly more than the pixel resolution of 150 m in the SAR images.

The decreasing accuracy can be related to an increase of melting during the campaign. The sea ice is very dynamic during the period, creating too many differences between the images. Large ice floes break into smaller pieces. The ice floes melt and get smaller, rotation increases, and the shapes of the ice floes are not preserved. From the satellite images it appears that the buoy floats within a streak of slush ice. Slush ice is even more difficult to track because the contours of an area of slush ice are constantly changing.

The buoy is able to make very accurate measurements of the ice drift, but it is limited to point measurements. It is uncertain how well the general performance of the drift algorithm corresponds to the accuracy that is determined at the specific position of the buoy.

6 References

[1] T. Grafström*, et al.*, "A summary of the ice season and icebreaking activities 2009/2010," SMHI and Sjöfartsverket, Norrköping, 2010.

[2] Swedish Meteorological and Hydrological Institute, "Ice conditions," sstcolor_20100414.pdf, Norrköping: SMHI, 2010.

[3] M. Thomas*, et al.*, "High resolution (400 m) motion characterization of sea ice using ERS-1 SAR imagery," *Cold Regions Science and Technology,* vol. 52, pp. 207-223, 2008.

[4] F. Pla and M. Bober, "Estimating translation/deformation motion through phase correlation," in *Image Analysis and Processing*, A. Del Bimbo, Ed., Berlin/New York: Springer-Verlag, 1997, pp. 653-660.

[5] D. Casasent and D. Psaltis, "Position, rotation, and scale invariant optical correlation," *Applied Optics,* vol. 15, pp. 1795-1799, 1976.

[6] B. S. Reddy and B. Chatterji, "An FFT-based technique for translation, rotation, and scale-invariant image registration," *IEEE Transactions on Image Processing* vol. 5, pp. 1266-1271, 1996.

[7] M. McGuire, "An image registration technique for recovering rotation, scale and translation parameters," *NEC Res. Inst. Tech. Rep., TR,* pp. 98-018, 1998.

[8] L. Yin*, et al.*, "Weighted median filters: a tutorial," *IEEE Transactions on Circuits and Systems II: Analog and Digital Signal Processing,* vol. 43, pp. 157-192, 1996.

[9] P. Wessel and W. H. F. Smith, "A global, self-consistent, hierarchical, high-resolution shoreline database," *Journal of Geophysical Research,* vol. 101, pp. 8741-8743, 1996.

7 Acknowledgments

This work has been funded by the Swedish National Space Board through the project ClimatIce, Dnr 113/09. The project to develop and build the buoy was mainly funded by the Swedish Maritime Administration. FDS Mätteknik AB is acknowledged for preparing the buoy and for giving support regarding the data connection. The buoy was flown to its starting position by a helicopter from Lapplandsflyg. The Finnish Coast Guard is acknowledged for taking care of the buoy and shipping it back to Sweden.

8 Appendix

List of transmitted parameters

1	Logger ID
2	Year
3	Day of year
4	Time of day
5	Time of day, 2nd
6	Latitude (1” precision)
7	Latitude (1e-4” precision)
8	Longitude (1” precision)
9	Longitude (1e-4” precision)
10	Temperature 1
11	Temperature 2
12	Temperature 3
13	PR
14	Pitch
15	Roll
16	Yaw
17	Battery voltage